ACCSCIENCE PUBLISHING

Asian Journal of Water, Environment and Pollution

ORIGINAL RESEARCH ARTICLE

Numerical investigation of nonlinear heat and mass transfer in Carreau hybrid nanofluid flow over an expanding cylinder with homogeneous–heterogeneous reactions

Karthik Velusamy[1], Asaigeethan Palanisamy[2]*, Shageen Fathima Shahul[1], and Priya Arunkumar[3]*

[1]Department of Industrial Biotechnology, Government College of Technology, Coimbatore, Tamil Nadu, India

[2]Department of Mathematics, Government College of Engineering, Erode, Tamil Nadu, India

[3]Division of Biotechnology, Karunya Institute of Technology and Sciences, Coimbatore, Tamil Nadu, India

Abstract

Recent advancements in nanofluids have significantly enhanced heat and mass transfer performance in complex engineering systems. In particular, hybrid nanofluids combined with non-Newtonian models have emerged as effective solutions for improving thermal efficiency under diverse physical conditions. The current study presents a combined investigation of Carreau hybrid nanofluid flow over an expanding cylinder with viscous dissipation, thermal radiation, and simultaneous homogeneous–heterogeneous reactions, providing a unified framework for analyzing coupled heat and mass transfer characteristics. Olive oil is employed as a biocompatible base fluid due to its high bioavailability and stability, while yttrium oxide (Y_2O_3) and zirconium oxide ZrO_2 nanoparticles are introduced to enhance thermophysical properties. The Carreau model is used to capture the shear-thinning behavior of the non-Newtonian fluid. The governing partial differential equations are transformed into a system of ordinary differential equations via similarity transformations and solved numerically using MATLAB's boundary value problem solver (bvp5c). The influence of key parameters, including the Weissenberg number, curvature parameter, Prandtl number, Schmidt number, Brownian motion, and thermophoresis, on the velocity, temperature, and concentration profiles was thoroughly analyzed. Results reveal that hybrid nanofluids significantly outperformed conventional nanofluids in heat and mass transfer efficiency, particularly under high curvature and viscoelastic conditions. The enhanced thermal performance and controllable diffusion characteristics of the hybrid nanofluid make it a promising candidate for applications in biomedical drug delivery systems and advanced thermal management technologies.

Keywords: Carreau hybrid nanofluid; Expanding cylinder; Heat transfer; Viscous dissipation; Homogeneous–heterogeneous reactions; Brownian motion; Thermophoresis; MATLAB bvp5c

***Corresponding authors:**
Asaigeethan Palanisamy (asaigeethan14@gct.ac.in);
Priya Arunkumar (akpriya@karunya.edu)

Citation: Velusamy K, Palanisamy A, Shahul SF, Arunkumar P. Numerical investigation of nonlinear heat and mass transfer in Carreau hybrid nanofluid flow over an expanding cylinder with homogeneous–heterogeneous reactions. *Asian J Water Environ Pollut.* 2026;23(5):026290193. doi: 10.36922/AJWEP026290193

Received: July 13, 2026

Revised: August 11, 2026

Accepted: August 12, 2026

Published online: September 4, 2026

Copyright: © 2026 Author(s). This is an Open-Access article distributed under the terms of the Creative Commons Attribution License, permitting distribution, and reproduction in any medium, provided the original work is properly cited.

Publisher's Note: AccScience Publishing remains neutral with regard to jurisdictional claims in published maps and institutional affiliations.

1. Introduction

Hybrid nanofluids composed of a base fluid containing more than one type of nanoparticle

exhibit enhanced thermal conductivity, stability, and heat transfer performance compared to conventional nanofluids. Their exceptional capabilities have made them valuable in various applications such as electronic cooling systems, solar collectors, and heat exchangers, where nonlinear convective flows play a critical role.[1-3] Numerous experimental and numerical studies have demonstrated that hybrid nanofluids outperform mono-nanofluids in terms of heat transfer, boiling performance, and thermal energy storage.[4,5] Among the available non-Newtonian fluid models, the Carreau model is selected in the present study because of its ability to describe shear-dependent viscosity over a broad range of shear rates. The model captures the limiting Newtonian behavior at low and high shear rates while representing shear-thinning behavior in the intermediate regime. Although Casson and Williamson models are also widely employed for non-Newtonian flow analysis, their rheological descriptions are more restricted to particular classes of shear-dependent fluids. Hence, the Carreau model provides greater flexibility for describing the complex rheological characteristics of the hybrid nanofluid considered in the present investigation.[6] This is particularly important in complex flow environments such as biomedical systems, where fluids experience varying shear rates.[7] When nanoparticles are introduced into Carreau fluids, the resulting Carreau nanofluid exhibits enhanced thermal performance while maintaining its non-Newtonian rheology.[8] The inclusion of magnetic fields, thermal radiation, and slip conditions further enriches the physical complexity of such flows, making them suitable for advanced simulations.[9,10]

Recent studies have explored magnetohydrodynamic (MHD) Carreau nanofluid flows over stretching surfaces, highlighting the importance of Brownian motion and thermophoresis effects on heat and mass transfer.[11-13] These effects are particularly relevant in microscale and biomedical systems, where particle migration significantly influences thermal behavior.[14,15] Researchers have also investigated the impact of activation energy, chemical reactions, and heat generation/absorption on Carreau nanofluid flows in porous and deformable media.[16-18]

A unique and promising area of research involves combining Carreau hybrid nanofluids with homogeneous–heterogeneous chemical reactions. These reactions, which occur simultaneously in both the bulk and surface phases, are highly relevant in catalytic systems and porous media.[19-21] Such systems have been studied over various geometries, including stretching sheets and curved surfaces, to simulate real-world applications such as polymer extrusion, coating processes, and drug delivery.[22-25]

The MHD second-grade nanofluid flow over a stretching circular cylinder was investigated with chemical reaction and slip effects, revealing that the magnetic parameter reduces velocity, while slip effects enhance temperature and concentration profiles.[26] Computational analysis of steady and oscillating heat and mass transfer in $MnZnFe_2O_4$–water nanofluid was performed considering exothermic reaction, solar radiation, magnetic field, and activation energy. The results showed that increasing buoyancy force and nanoparticle volume fraction enhance heat and mass transfer, while a stronger exothermic reaction increases temperature oscillations. Activation energy, solar radiation, reaction rate, and nanoparticle concentration substantially influence the oscillating nanofluid flow.[27] Mixed convection heat and mass transfer of graphene oxide–water Maxwell nanofluid over a radiating cylinder was investigated under steady and unsteady conditions. The results showed that the Maxwell parameter increases velocity, temperature, and concentration, while radiation intensifies oscillations in velocity and temperature.[28] MHD Oldroyd-B fluid flow over a stretching polymeric surface was investigated considering viscous dissipation, variable density, Soret and Dufour effects, and convective boundary conditions. The results showed that increasing the magnetic field enhances temperature, whereas increasing the Prandtl number (Pr) reduces it. Higher convective heat-transfer parameters also increase skin friction and mass-transfer rates.[29]

Carreau ternary hybrid nanofluid stagnation-point flow over a stretching cylinder incorporating thermal diffusion and molecular motion effects, confirming enhanced thermal and solutal transport over conventional nanofluid models, a finding consistent with the recent study's approach.[30] Homogeneous–heterogeneous surface reactions and magnetic retardation in an Al_2O_3-Cu hybrid nanofluid over a stretching cylinder significantly intensify species depletion at the catalytic wall, a mechanism analogous to the Damköhler-number-driven pollutant degradation modeled has been investigated.[31] The internal heat generation and nonlinear buoyancy forces jointly amplify thermal transport in porous medium flows, a finding consistent with the role of the heat generation parameter observed in the present penta-hybrid nanofluid system.[32] The penta-hybrid nanofluids composed of five distinct nanoparticles in a blood-based fluid under MHD squeezing flow deliver superior thermal performance compared to lower-order hybrid formulations, validating the motivation for adopting a penta-hybrid nanofluid.[33]

Olive oil is selected as the base fluid for the current Carreau hybrid nanofluid because of its biocompatibility, low toxicity, thermal stability, and potential relevance to biomedical heat-transfer applications. Yttrium oxide $\left(Y_2O_3\right)$ and zirconium oxide ZrO_2 nanoparticles are incorporated to enhance thermal transport and mass

diffusion characteristics. Although previous studies have examined Carreau nanofluids, hybrid nanofluids, and homogeneous–heterogeneous reactions separately, their combined effects over an expanding cylinder remain insufficiently explored. Therefore, the present study investigates the nonlinear convective flow of a Y_2O_3-ZrO_2/ olive oil Carreau hybrid nanofluid over an expanding cylinder, considering viscous dissipation, thermal radiation, Brownian motion, thermophoresis, and homogeneous–heterogeneous reactions. The study aims to clarify the coupled momentum, heat, and mass-transfer characteristics, thereby addressing the identified research gap.

2. Mathematical formulation

We considered the steady, axisymmetric flow of a Carreau hybrid nanofluid over a stretching cylinder in the presence of a uniform transverse magnetic field. The mathematical model incorporated viscous dissipation, Brownian motion, thermophoresis, and homogeneous–heterogeneous chemical reactions. The Buongiorno model was adopted to characterize nanoparticle transport by accounting for Brownian diffusion and thermophoretic effects. Figure 1 shows the materialistic representation and coordinate system. Table 1 shows the important thermal properties of selected nanoparticles used in the study.

A single-step isothermal reaction was considered between species A and B, governed by first-order kinetics (**Equations 1** and **2**).

$$A + 2B \rightarrow 3B, \qquad rate = d_c ab^2 \tag{1}$$

Table 1. Important thermal properties of selected nanoparticles used in the study[34,35]

Nanoparticles	Thermal properties		
	$C_p\left(Jkg^{-1}K^{-1}\right)$	$\rho\left(kgm^{-3}\right)$	$k\left(Wm^{-1}K^{-1}\right)$
Y_2O_3	0.466×10^3	5,010	14.5
ZrO_2	0.502×10^3	5,680	1.7
C_nH_{2n+2}	2,000	920	0.168

Abbreviations: Y_2O_3: yttrium oxide; ZrO_2: Zirconium oxide.

On the catalyst surface, a first-order single-reaction process was thermodynamically proceeding.

$$A \rightarrow B, \qquad rate = d_s a \tag{2}$$

The concentrations of chemicals A and B for the species combination were expressed as a and b, respectively, while the rate constants d_c and d_s were indicated, assuming that both were isothermal reaction processes. The model's governing equations were constructed after applying the common boundary-layer approximations.

$$\frac{\partial}{\partial x}(ru) + \frac{\partial}{\partial r}(rv) = 0 \tag{3}$$

$$u\frac{\partial u}{\partial x} + v\frac{\partial u}{\partial r} = \frac{\mu_{hnf}}{\rho_{hnf}}\frac{1}{r}\frac{\partial}{\partial r}\left[\left(r\frac{\partial u}{\partial r}\right)\left(1+\Gamma^2\left(\frac{\partial u}{\partial r}\right)^2\right)\right]^{\frac{n-1}{2}} + \frac{\mu_{hnf}}{\rho_{hnf}}(n-1)\Gamma^2\frac{\partial^2 u}{\partial r^2}\left(\frac{\partial u}{\partial r}\right)^2\left[1+\Gamma^2\left(\frac{\partial u}{\partial r}\right)^2\right]^{\frac{n-3}{2}} - \frac{\sigma_{hnf}B_0^2 u}{\rho_{hnf}}, \tag{4}$$

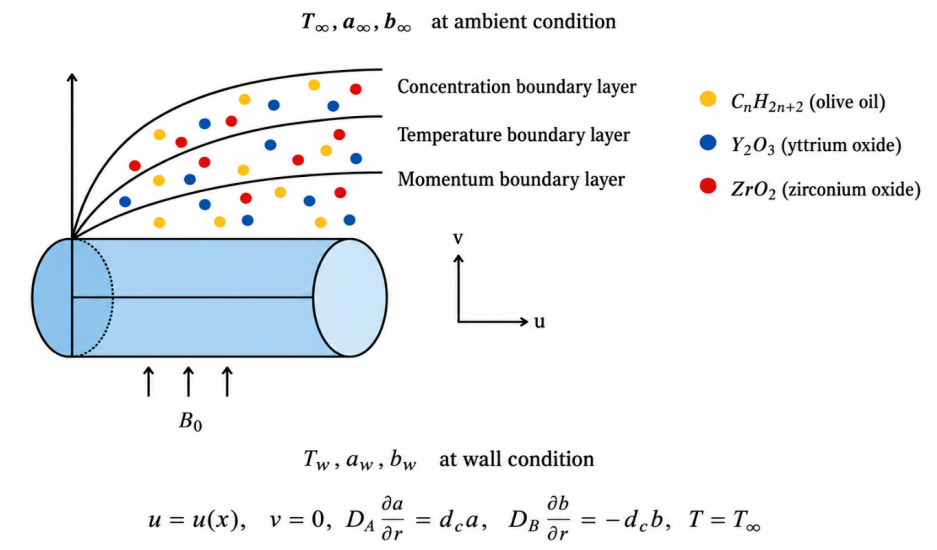


Figure 1. The materialistic representation and coordinate system

$$u\frac{\partial T}{\partial x}+v\frac{\partial T}{\partial r}=\frac{k_{hnf}}{r\left(\rho C_p\right)_{hnf}}\frac{\partial}{\partial r}\left[r\frac{\partial T}{\partial r}\right]+\tau\left[D_B\frac{\partial a}{\partial r}\frac{\partial T}{\partial r}+\frac{D_T}{T_\infty}\left(\frac{\partial T}{\partial r}\right)^2\right], \quad (5)$$

$$u\frac{\partial a}{\partial x}+v\frac{\partial a}{\partial r}=D_A\left[\frac{\partial^2 a}{\partial r^2}+\frac{\partial a}{\partial r}\right]+D_A\frac{\partial a}{\partial r}+\frac{D_T}{T_\infty}\frac{\partial T}{\partial r}-d_c ab^2, \quad (6)$$

$$u\frac{\partial b}{\partial x}+v\frac{\partial b}{\partial r}=D_B\left[\frac{\partial^2 b}{\partial r^2}+\frac{\partial b}{\partial r}\right]+D_B\frac{\partial b}{\partial r}+\frac{D_T}{T_\infty}\frac{\partial T}{\partial r}+d_s ab^2, \quad (7)$$

Based on **Equations 3–7**, the boundary conditions are stated as follows (**Equation 8**):

$$\begin{aligned}&u=u(x), v=0,\ D_A\frac{\partial a}{\partial r}=d_c a,\ D_B\frac{\partial b}{\partial r}=-d_s a,\\&T=T_w,\ D_A\frac{\partial a}{\partial r}+\frac{D_T}{T_\infty}\frac{\partial T}{\partial r}=0,\ D_B\frac{\partial b}{\partial r}+\frac{D_T}{T_\infty}\frac{\partial T}{\partial r}=0\ at\ r=R,\\&u\to 0,\ T\to T_\infty,\ a\to a_\infty,\ b\to b_\infty\ at\ r\to\infty\end{aligned} \quad (8)$$

The stretching velocity of the cylinder is defined as $u(x)=\frac{xu_0}{l}$, where u_0 denotes the characteristic stretching velocity, and l is the characteristic length. The velocity components u and v represent the axial and radial velocities, respectively. The concentrations of the chemical species A and B are denoted as a and b, while D_A and D_B denote their respective mass diffusivities. The thermophysical properties of the hybrid nanofluid include density ρ_{hnf}, dynamic viscosity μ_{hnf}, kinematic viscosity ν_{hnf}, specific heat capacity $\left(C_p\right)_{hnf}$, volumetric heat capacity $\left(\rho C_p\right)_{hnf}$, thermal conductivity k_{hnf}, and thermal diffusivity α_{hnf}. The parameter n denotes the power-law index in the adopted constitutive model. At the cylinder surface, the zero nanoparticle mass-flux condition is imposed to account for Brownian diffusion and thermophoretic migration.

2.1. Effective thermophysical properties of the hybrid nanofluid

The effective thermophysical properties of the $Y_2O_3-ZrO_2$ / olive oil hybrid nanofluid were evaluated using conventional mixture and effective-medium correlations. The effective density and heat capacity were determined from the volumetric mixture relations, while the effective viscosity was calculated using the Brinkman-type relation. The effective thermal conductivity was obtained using a sequential Maxwell-type model, in which the effective conductivity of the first nanoparticle base-fluid suspension was calculated first and subsequently used as the effective base conductivity for the second nanoparticle. Accordingly, the effective properties are expressed as follows (**Equations 9–13**):

- Effective density

$$\frac{\rho_{hnf}}{\rho_f}=\left(1-\varphi_{Y_2O_3}\right)\left[1-\varphi_{Y_2O_3}+\varphi_{Y_2O_3}\frac{\rho_{Y_2O_3}}{\rho_f}\right]+\varphi_{ZrO_2}\frac{\rho_{Ag}}{\rho_f} \quad (9)$$

- Effective viscosity

$$\frac{\mu_{hnf}}{\mu_f}=\frac{1}{\left(1-\varphi_{Y_2O_3}\right)^{2.5}\left(1-\varphi_{ZrO_2}\right)^{2.5}} \quad (10)$$

- Effective heat capacity

$$\frac{\left(\rho C_p\right)_{hnf}}{\left(\rho C_p\right)_f}=\left(1-\varphi_{ZrO_2}\right)\left[1-\varphi_{Y_2O_3}+\varphi_{Y_2O_3}\frac{\left(\rho C_p\right)_{Y_2O_3}}{\left(\rho C_p\right)_f}\right]+\varphi_{ZrO_2}\frac{\left(\rho C_p\right)_{ZrO_2}}{\left(\rho C_p\right)_f} \quad (11)$$

- Effective thermal conductivity

$$\frac{k_{hnf}}{k_f}=\frac{k_{ZrO_2}+2k_{bf}+2\varphi_{ZrO_2}\left(k_{ZrO_2}-k_f\right)}{k_{ZrO_2}+2k_{bf}-2\varphi_{ZrO_2}\left(k_{ZrO_2}-k_f\right)}, \quad (12)$$

where $\frac{k_{bf}}{k_f}=\frac{k_{Y_2O_3}+2k_f+2\varphi_{Y_2O_3}\left(k_{Ag}-k_f\right)}{k_{Y_2O_3}+2k_f-2\varphi_{Y_2O_3}\left(k_{Ag}-k_f\right)}$,

$$\alpha_{hnf}=\frac{k_{hnf}}{\left(\rho C_p\right)_{hnf}} \quad (13)$$

Olive oil was used as the base fluid for the present Carreau hybrid nanofluid, with Y_2O_3 and ZrO_2 nanoparticles dispersed in it. The nanoparticle volume fractions of Y_2O_3 and ZrO_2 were denoted by $\varphi_{Y_2O_3}$ and φ_{ZrO_2}, respectively. In the present study, both nanoparticles were used at a volume fraction of 3%, i.e., $\varphi_{Y_2O_3}=\varphi_{ZrO_2}=0.03$, these concentrations were selected to enhance the effective thermal conductivity of the hybrid nanofluid while maintaining stable nanoparticle dispersions and limiting excessive particle agglomerations. The total hybrid nanoparticle volume fraction was therefore $\varphi_{Y_2O_3}+\varphi_{ZrO_2}=0.06$. When $\varphi_{Y_2O_3}=\varphi_{ZrO_2}=0$, the hybrid nanofluid reduced to the base Carreau fluid.

The stream function $\psi(r,x)$ is presented to attempt to conclude the continuity equation (**Equation 14**), such that:

$$u=\frac{1}{r}\frac{\partial\psi}{\partial r},\quad v=-\frac{1}{r}\frac{\partial\psi}{\partial x} \quad (14)$$

where $\psi=\sqrt{u(x)\nu_f x}\ Rf(\eta)$,

The dimensionless stream function is shown as **Equation 15**:

$$\eta=\frac{r^2-R^2}{2R}\sqrt{\frac{u(x)}{\nu_f x}},\quad \theta(\eta)=\frac{T-T_\infty}{T_p-T_\infty} \quad (15)$$

The chemical concentration calculations for species A and B are shown in **Equation 16**:

$$m(\eta)=\frac{a}{a_0} \text{ and } n(\eta)=\frac{b}{b_0} \tag{16}$$

The governing equations assume the following form after integrating the designated transformation (**Equations 17–20**):

$$\begin{aligned}&2D_1k\left(1+we^2\left(f''\right)^2\right)^{\frac{n-1}{2}}\\&+D_1\left(1+2k\eta\right)f'''\left(1+we^2\left(f''\right)^2\right)^{\frac{n-1}{2}}\\&D_1\left(n-1\right)we^2\left(f''\right)^3k(1+we^2\left(f''\right)^2)^{\frac{n-3}{2}}\\&D_1\left(n-1\right)we^2\left(f''\right)^2f'''\left(1+we^2\left(f''\right)^2\right)^{\frac{n-3}{2}}\left(1+2k\eta\right)\\&-D_2Bf'-\left(f'\right)^2+ff''=0,\end{aligned} \tag{17}$$

$$\begin{aligned}&D_4\left(1+2k\eta\right)\theta''+2kD_3\theta'+D_3Prf\theta'\\&+\left(1+2k\eta\right)\left[N_bm'.\theta'+N_t\left(\theta'\right)^2\right]=0,\end{aligned} \tag{18}$$

$$\begin{aligned}&\frac{1}{Sc}\left(\left(1+2k\eta\right)m''+2km'\right)+m'f\\&+\frac{N_t}{N_b}\left[\left(1+2k\eta\right)\theta''\left(\eta\right)+2k\ \theta'\right]-Lmn^2=0,\end{aligned} \tag{19}$$

$$\begin{aligned}&\frac{\delta}{Sc}\left(\left(1+2k\eta\right)n''+2kn'\right)+n'f\\&+\frac{N_t}{N_b}\left[\left(1+2k\eta\right)\theta''\left(\eta\right)+2k\ \theta'\right]+Lmn^2=0,\end{aligned} \tag{20}$$

The corresponding boundary conditions are shown in **Equation 21**:

$$\begin{aligned}&f\left(0\right)=0,f'\left(0\right)=1,\ \theta\left(0\right)=1,\ m'\left(0\right)=L_sm\left(0\right),\\&N_bm'\left(0\right)+N_t\theta'\left(0\right)=0,\ \delta n'\left(0\right)=\frac{-Lsn\left(0\right)}{\nu_f},\\&f'\left(\infty\right)=0,\ \theta\left(\infty\right)=0,\ \left(\infty\right)=1,\ n\left(\infty\right)=1.\end{aligned} \tag{21}$$

The curvature parameter k, the Weissenberg number We, magnetic field parameter B, Pr, Schmidt number Sc, ratio diffusion coefficients δ, the diffusive transport limiting factor N_b, the thermally-driven migration limiting factor N_t, and the homogeneous–heterogeneous reactions limiting factor Ls are all constants that have no dimensions in **Equations 17–21**; their typical expressions are shown in Table 2.

Table 2. Typical expressions of parameters from Equations 17–21

Parameter	Symbol	Expression
Curvature parameter	k	$\frac{1}{R}\sqrt{\frac{\nu_f l}{u_0}}$
Weissenberg number	We	$\frac{\tau^2r^2u_0^3x^2}{l^3\nu_f}$
Magnetic field parameter	B	$\frac{\sigma_fB_0^2}{\rho_fa}$
Prandtl number	Pr	$\frac{\nu_f}{\alpha}$
Schmidt number	Sc	$\frac{\nu_f}{D_A}$
Ratio diffusion coefficients	δ	$\frac{D_B}{D_A}$
Brownian motion limiting factor	N_b	$\frac{\tau D_B\left(b_w-b_\infty\right)}{\nu}$
Thermophoresis limiting factor	N_t	$\frac{\tau D_T\left(T_w-T_\infty\right)}{\nu T_\infty}$
Homogeneous–heterogeneous reactions limiting factor	Ls	$\frac{l_s}{D_A}\sqrt{\frac{\nu_f l}{u_0}}$
Effective dynamic viscosity parameter	D_1	$\frac{1}{[(1-\varphi_1)^{2.5}(1-\varphi_2)^{2.5}](1-\varphi_2)\left[1-\varphi_1+\varphi_1\frac{\rho_{s1}}{\rho_f}\right]+\varphi_2\frac{\rho_{s2}}{\rho_f}}$
Effective density parameter	D_2	$\frac{1}{\left(1-\varphi_2\right)\left[1-\varphi_1+\varphi_1\frac{\rho_{s1}}{\rho_f}\right]+\varphi_2\frac{\rho_{s2}}{\rho_f}}$
Effective heat capacity parameter	D_3	$\left(1-\varphi_2\right)\left[1-\varphi_1+\varphi_1\frac{\left(\rho C_p\right)_{s1}}{\left(\rho C_p\right)_f}\right]+\varphi_2\frac{\left(\rho C_p\right)_{s2}}{\left(\rho C_p\right)_f}$
Effective thermal conductivity parameter	D_4	$\frac{k_{s2}+2k_{bf}+2\varphi_2\left(k_{s2}-k_f\right)}{k_{s2}+2k_{bf}-2\varphi_2\left(k_{s2}-k_f\right)}$

Chemicals A and B typically have variables of diffusion that are about analogous in size. Assuming that D_A and D_B are equal $(i.e., \delta = 1)$; hence (**Equation 22**):

$$m(\eta) + n(\eta) = 1 \tag{22}$$

Equations 19 and **20** thus become **Equation 23**:

$$\frac{1}{Sc}\left((1+2k\eta)m'' + 2km'\right) + m'f + \frac{N_t}{N_b}\left[(1+2k\eta)\theta'' + 2k\theta'\right] - Lm(1-m)^2 = 0 \tag{23}$$

The boundary conditions then influence **Equation 24**:

$$m'(0) = Lsm(0),\ m(\infty) \to 1 \tag{24}$$

3. Physical quantities

The engineering quantities of interest, namely the skin friction coefficient, Nusselt number, and Sherwood number, are evaluated to analyze the flow, heat, and mass transfer behavior. These parameters provide a quantitative measure of the surface drag, thermal performance, and species diffusion characteristics of the hybrid nanofluid system.

- Coefficient of skin friction

The coefficient of boundary-layer drag C_f is the pertinent physical parameter. It describes surface drag, which is given by the stress caused by shearing at the wall surface τ_{rx} (**Equation 25**).

$$\tau_{rx} = -\mu_{hnf}\left(\left(\frac{\partial u}{\partial r}\right)\left[1 + \Gamma^2\left(\frac{\partial u}{\partial r}\right)^2\right]^{\frac{n-1}{2}}\right)_{r=R} = -D_2 f''(0)\left(1 + we^2\left(f''(0)\right)^2\right)^{\frac{n-1}{2}} \tag{25}$$

Here, μ_{hnf} is the viscous modulus of the Carreau hybrid nanofluid, and the coefficient of boundary-layer drag is defined as **Equation 26**:

$$C_f = \frac{2(\tau_{rx})_{r=R}}{\rho_f u(x)^2} \tag{26}$$

Using **Equations 25** and **26**, **Equation 27** can be derived:

$$C_f\sqrt{Re_x} = -2D_2 f^{"}(0)\left(1 + we^2\left(f''(0)\right)^2\right)^{\frac{n-1}{2}} \tag{27}$$

- Nusselt number

The local Nusselt number Nu is the physical amount of significance, given by the heat transfer at the wall's surface q_w (**Equation 28**):

$$q_w = -k_{hnf}\left(\frac{\partial T}{\partial r}\right)_{r=R} \tag{28}$$

The local *Nu* is given by **Equation 29**:

$$Nu = \frac{(xq_w)_{r=R}}{k(T_p - T_\infty)} \tag{29}$$

Substituting **Equation 28** in **Equation 29**, we obtained **Equation 30**:

$$\frac{Nu}{\sqrt{Re_x}} = -D_4\theta'(0) \tag{30}$$

- Sherwood number

The local Sherwood number Sh is the pertinent physical quantity, given by the wall's mass-motion surface q_m. (**Equation 31**):

$$q_m = -D\left(\frac{\partial m}{\partial r}\right)_{r=R} \tag{31}$$

The local *Sh* is given by **Equation 32**:

$$Sh = \frac{(xq_m)_{r=R}}{D(C_p - C_\infty)} \tag{32}$$

Substituting **Equation 31** into **Equation 32**, we obtained **Equation 33**:

$$\frac{Sh}{\sqrt{Re_x}} = m'(0) \tag{33}$$

In **Equations 27, 30,** and **33**, Re_x represents the local Reynolds number defined by $Re_x = \frac{Xu(x)}{\nu_f}$.

4. Methodology

The governing **Equations 17, 18,** and **24** became highly nonlinear when the boundary conditions given by **Equations 21** and **24** were applied. To address the non-dimensionalized versions of these equations, a boundary-value-problem approach is used, with the function serving as the numerical method for solving them. Figure 2 illustrates the flow chart for the bvp5c process. The initial step involves converting **Equations 17, 18,** and **23** into first-order ordinary differential equations (**Equation 34**):

$$f = y_1,\ f' = y_2,\ f'' = y_3,\ f''' = y_3',\ \theta = y_4,\ \theta' = y_5,,\ \theta'' = y_5',\ m = y_6,\ m' = y_7,\ m'' = h_7' \quad (34)$$

Substituting **Equation 34** into **Equations 17, 18,** and **23**, they are converted to **Equations 35–37:**

$$H_1 = y_3' = \frac{y_2^2 - y_1 y_3 - 2D_1 k\left(1+we^2(y_3)^2\right)^{\frac{n-1}{2}} - D_1 k(n-1)we^2(y_3)^3\left(1+we^2(y_3)^2\right)^{\frac{n-3}{2}}}{D_1(1+2k\eta)\left(1+we^2(y_3)^2\right)^{\frac{n-1}{2}} + D_1(n-1)we^2 y_3^2(1+2k\eta)\left(1+we^2(y_3)^2\right)^{\frac{n-3}{2}}} \quad (35)$$

$$H_2 = y_5' = \frac{-D_3[2ky_5 + Pry_1y_5] - (1+2k\eta)[N_b y_5 y_7] + (1+2k\eta)[N_t(y_5)^2]}{D_4(1+2k\eta)} \quad (36)$$

$$H_2 = h_5' = \frac{Ly_6(1-y_6)^2 - 2ky_7 - y_1y_7 - \frac{N_t}{N_b}(1+2k\eta)[2ky_5]}{\frac{1}{S_c}(1+2k\eta)} \quad (37)$$

With boundary conditions shown in **Equation 38**:

$$\begin{aligned} &y_1(0) = 0, y_2(0) = 1, y_4(0) = 1, \\ &y_7(0) = Ls\ y_6(0), N_b y_7(0) + N_t y_5(0) = 0, \\ &y_2(\infty) = 0, y_4(\infty) = 0, y_6(\infty) = 1. \end{aligned} \quad (38)$$

In this case, the boundary value problem was performed to solve **Equations 35–37**, along with the corresponding boundary conditions from **Equation 38**. Initially, approximate initial values were selected for $y_3(0), y_5(0), and\ y_7(0)$ as –1, 1, and 1, respectively. Then, the resulting system of first-order ordinary differential equations was solved using the boundary value problem technique. The solution was iterated until the residuals of H_1, H_2 and H_3 fell within the acceptable error threshold, ensuring that the desired convergence criteria were met.

The boundary-value problem was solved using MATLAB's bvp5c solver (MATLAB R2024b, MathWorks, Inc., USA) with adaptive mesh refinement. The numerical solution was considered converged when the changes in the computed solution and engineering quantities between successive refinements were negligible and remained within the prescribed solver tolerance. A mesh-independence check was also performed by increasing the number of computational mesh points, and no significant variation was observed in the velocity, temperature, and concentration profiles. The solver tolerance was maintained at 10^{-6}, ensuring satisfactory numerical accuracy and stability. The converged solutions were subsequently used to calculate the skin-friction coefficient, *Nu*, and *Sh*.

Table 3 shows the effect of We and k on the performance of the nanofluid and hybrid nanofluid. The results show that hybrid nanofluids exhibited higher heat transfer performance than nanofluids as k and We increased.

Table 4 illustrates the impact of the Pr with k, Brownian motion parameter N_b, and thermophoretic parameter N_t on the performance of nanofluid and hybrid nanofluid. The hybrid nanofluid consistently performed well across varying parameters, highlighting its enhanced heat transfer capabilities.

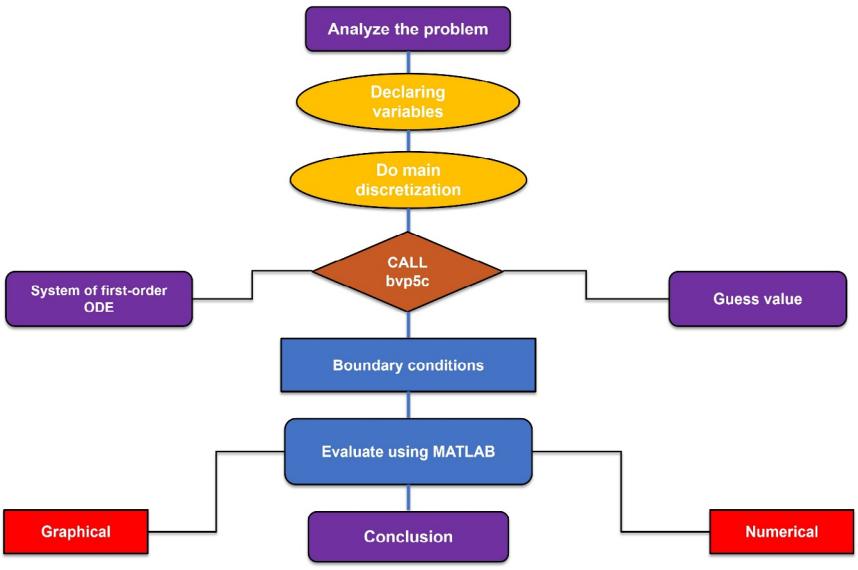


Figure 2. Algorithm flow sheet of the bvp5c technique
Abbreviation: ODE: Ordinary differential equation.

Table 3. Coefficients of skin friction for various values of We , k , and the fixed values of $Sc = 1.2$ and $Pr = 6$

We	k	Base fluid, $\varphi_1 = 0$, $\varphi_2 = 0$	Nanofluid, $\varphi_1 = 0.03$, $\varphi_2 = 0$	Hybrid nanofluid, $\varphi_1 = 0.03$, $\varphi_2 = 0.03$
0.3	0.5	1.7394	1.9549	2128
	0.6	1.9259	2.2073	2.2838
	0.8	2.3448	2.7830	2.9040
0.5	0.5	1.9300	2.2170	2.2896
	0.6	2.1749	2.5603	2.6602
0.7	0.5	2.1713	2.5449	2.6357

Abbreviations: k: Curvature parameter; Pr: Prandtl number; Sc: Schmidt number; We: Weissenberg number.

Table 4. Nusselt number for various values of Pr, k, N_b, N_t and the fixed values of $Sc = 1.2$ and $We = 3$

Pr	k	N_b	N_t	Base fluid, $\varphi_1 = 0$, $\varphi_2 = 0$	Nanofluid, $\varphi_1 = 0.03$, $\varphi_2 = 0$	Hybrid nanofluid, $\varphi_1 = 0.03$, $\varphi_2 = 0.03$
1	0.5	1.5	0.5	5.4856	5.9590	7.5438
	0.6	1.5	0.5	6.8702	7.5688	8.8701
	0.8	1.5	0.5	7.4569	8.7756	9.6833
2	0.5	1.6	0.75	5.4956	5.9698	7.5445
	0.5	1.7	0.75	6.4722	6.9244	8.2302
	0.5	1.6	0.6	5.5021	5.9788	7.5450
3	0.5	1.6	0.7	6.2322	6.9342	8.1021

Abbreviations: k: Curvature parameter; N_b: Brownian motion limiting factor; N_t: Thermophoresis limiting factor; Pr: Prandtl number; Sc: Schmidt number; We: Weissenberg number.

Table 5 depicts the influence of the homogeneous parameter Ls against Sc on nanofluid and hybrid nanofluid performance. The hybrid nanofluid demonstrated the highest performance improvement as Ls and Sc increase, reflecting enhanced transport properties.

The ranges of the governing dimensionless parameters were selected based on their physical significance and the ranges commonly adopted in related non-Newtonian hybrid nanofluid transport investigations. The selected values were restricted to physically meaningful regimes that preserve the validity of the mathematical model and provide stable numerical solutions. The parameter variations were selected to systematically examine the individual effects of the magnetic field, curvature, non-Newtonian characteristics, thermal radiation, Brownian motion, thermophoresis, and homogeneous–heterogeneous chemical reactions on the velocity, temperature, and concentration distributions. These ranges also enabled a meaningful assessment of the sensitivity of the transport characteristics and engineering quantities to the principal controlling parameters.

5. Results and discussion

MATLAB results show the effects of several factors on temperature, concentration, and velocity profiles. Under various physical circumstances, important outputs such as skin friction, Nusselt, and Sh were investigated.

- Velocity profile

As k increased, both nanofluids and hybrid nanofluids experienced a faster reduction in velocity due to more vigorous resistance to the motion (Figure 3A). The velocity profile $f'(\eta)$ decreased by about 20% at $\eta = 0.5$ as the reaction rate constant k rose from 0.3 to 0.5, with hybrid nanofluids consistently showing lower velocity than conventional nanofluids. The hybrid nanofluid demonstrated better flow stability and improved heat transfer, highlighting the benefits of using multiple nanoparticles for enhanced

Table 5. Sherwood number for various values of *Ls*, *Sc*, and the fixed values of $Pr = 6$ and $We = 3$

Ls	*Sc*	Base fluid, $\varphi_1 = 0$, $\varphi_2 = 0$	Nanofluid, $\varphi_1 = 0.03$, $\varphi_2 = 0$	Hybrid nanofluid, $\varphi_1 = 0.03$, $\varphi_2 = 0.03$
0.4	1.0	5.4856	6.1326	8.4153
	1.2	6.7237	7.2353	9.1287
	1.5	7.1236	9.3120	11.765
0.5	1.0	5.5038	6.4368	7.9874
	1.2	6.8974	7.6740	9.0975
0.6	1.0	5.6543	6.9875	8.9845

Abbreviations: *Ls*: Homogeneous–heterogeneous reactions limiting factor; *Pr*: Prandtl number; *Sc*: Schmidt number; *We*: Weissenberg number.

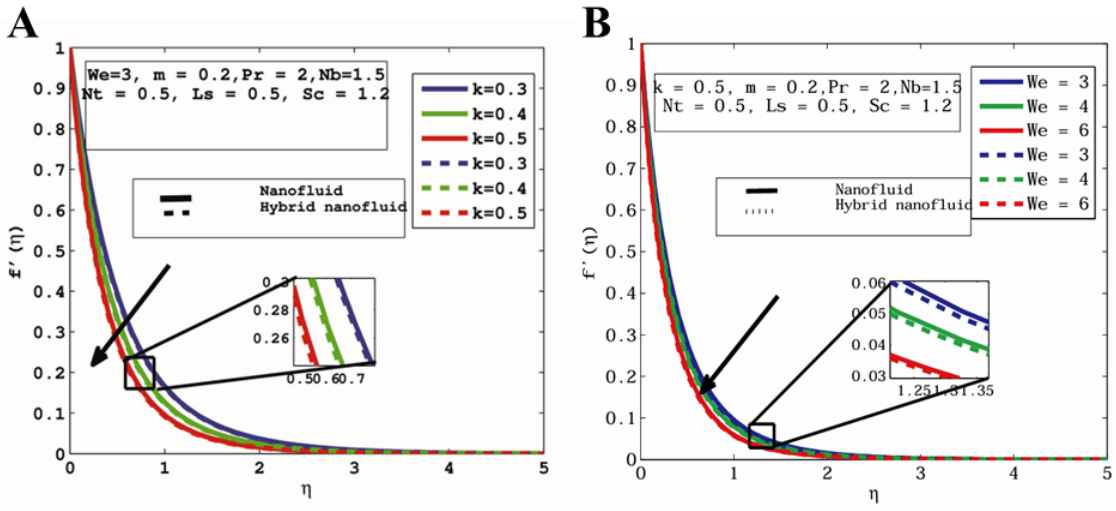


Figure 3. Effect on the velocity at (A) *k* and (B) *We*
Abbreviations: *k*: curvature parameter; *Ls*: Homogeneous–heterogeneous reactions limiting factor; N_b: Brownian motion limiting factor; N_t: Thermophoresis limiting factor; *Pr*: Prandtl number; *Sc*: Schmidt number; *We*: Weissenberg number.

performance under varying conditions. It is noteworthy that increased *k* would increase the centrifugal forces acting on the fluid, thereby amplifying resistance and disrupting the flow.

As *We* increased, the velocity decreased rapidly, indicating greater resistance due to viscoelastic effects (Figure 3B). The velocity gradient $f'(\eta)$ at $\eta = 1.3$ decreased by about 40% when *We* increased from 3 to 6. Hybrid nanofluids regularly exhibited lower values than nanofluids. However, the hybrid nanofluid exhibited greater moment flow stability than the nanofluid, consistent with studies that highlight its improved heat transfer efficiency under complex conditions. This is because a higher *We* reflects excellent elasticity in the fluid, which resists deformation and slows the flow.

- Temperature profile

The increase in *Pr* resulted in a rapid decrease in temperature (Figure 4A). At η = 0.8, the temperature profile (η) decreased by around 20% as the *Pr* rose from 2 to 5. Hybrid nanofluids consistently maintained lower temperatures than conventional nanofluids. The temperature profiles of nanofluids and hybrid nanofluids were highly similar, indicating that the hybrid nanofluid's thermal properties closely resemble those of the nanofluid. The reason may be that fluids with higher *Pr* values tend to have greater resistance to heat diffusion, resulting in quicker temperature drops.

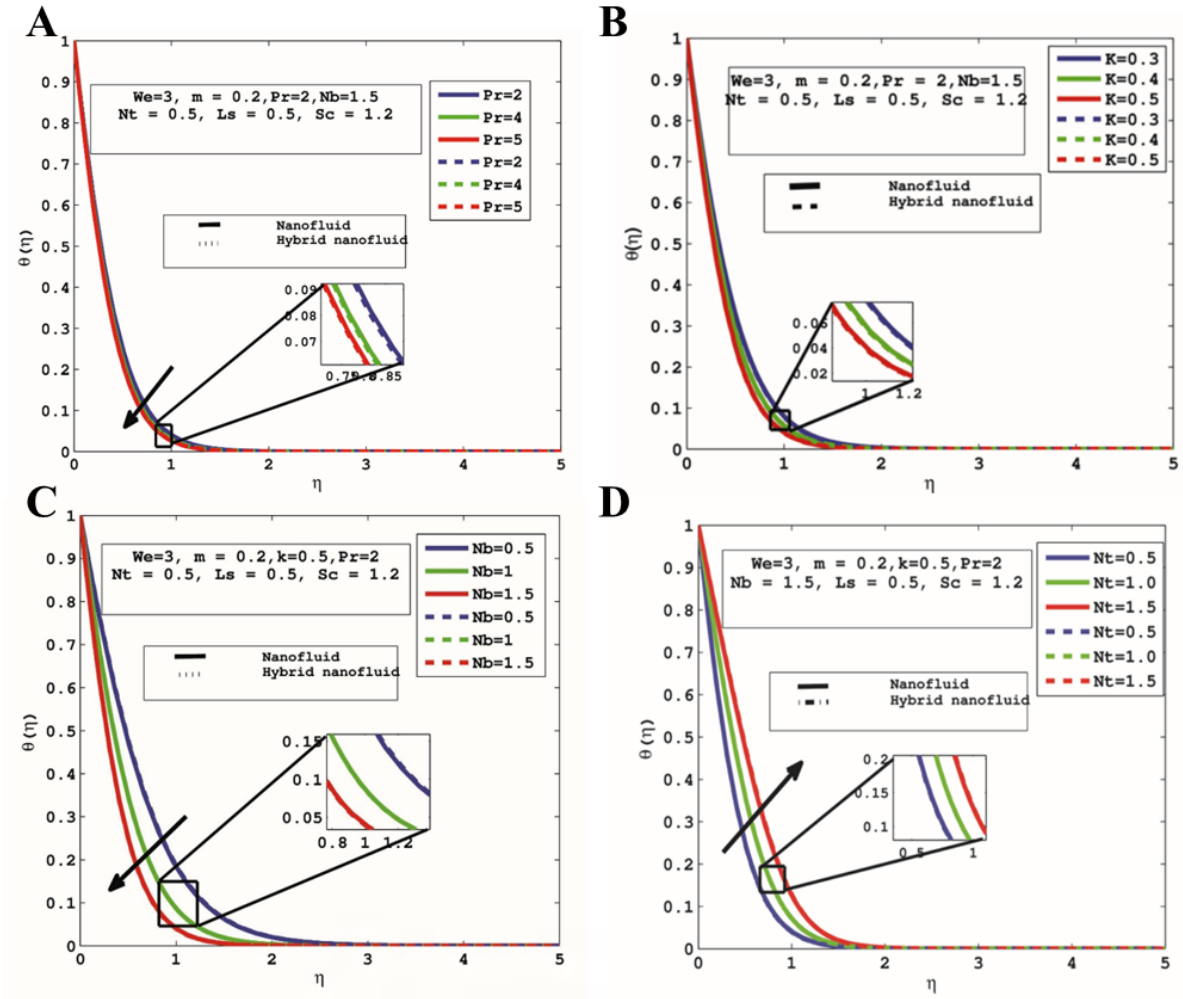


Figure 4. The effect on temperature at (A) *Pr*, (B) *k*, (C) N_b, (D) N_t
Abbreviations: *k*: curvature parameter; *Ls*: Homogeneous–heterogeneous reactions limiting factor; N_b: Brownian motion limiting factor; N_t: Thermophoresis limiting factor; *Pr*: Prandtl number; *Sc*: Schmidt number; *We*: Weissenberg number.

Figure 4B shows that as the *k* increased, the temperature profile decreased. The temperature profile (η) at η = 1.1 decreased by about 35% when the reaction rate constant increased from 0.3 to 0.5. Hybrid nanofluids regularly showed lower temperatures than nanofluids. This is because a higher *k* enhances convective heat transfer by promoting greater interaction between the fluid layers and the surface. Generally, heat transfer in hybrid nanofluids was better at lower temperatures, and vice versa.

When N_b increased, the temperature decreased rapidly. In other words, higher N_b values in hybrid nanofluids resulted in lower temperature (Figure 4C). The temperature profile $\theta(\eta)$ at η = 0.5 decreased by almost 60% when N_b increased from 0.5 to 1.5, with hybrid nanofluids continuously retaining lower temperatures than nanofluids. It should be noted that the N_b represents the random motion of nanoparticles within the fluid that enhances energy exchange between the nanoparticles and the surrounding fluid.

Generally, the thermophoresis parameter (N_t) quantifies the motion of nanoparticles due to temperature gradients. Figure 4D shows that as the N_t increased, the temperature decreased more slowly. As N_t increased, the temperature profile drops more quickly, and the hybrid nanofluid exhibits a thermal boundary layer thickness that is about 18% more than that of the nanofluid. The hybrid nanofluid consistently exhibits slightly lower temperatures than the nanofluids. As N_t increases, nanoparticles migrate from higher- to lower-temperature regions, reducing the local concentration of nanoparticles in hotter areas. The results reveal that the hybrid nanofluid exhibits better heat transfer performance.

- Concentration profile

Figure 5A shows the effect of *Sc* on the concentration for nanofluids and hybrid nanofluids. The concentration profile rose as *Sc* increased, and at *Sc* = 0.8, the hybrid nanofluid showed a concentration that was nearly 10% higher than the nanofluid. Hybrid nanofluids exhibited slightly higher concentration values due to the presence of multiple types of nanoparticles. Therefore, it can create a more stable suspension with reduced agglomeration.

Figure 5B depicts the effect of *Ls* on the concentration profile for nanofluids and hybrid nanofluids. The *Ls* represents the influence of a chemical reaction or source/sink term on mass transfer. As the Lewis number rose, the concentration profile fell, and at *Ls* = 0.4. The hybrid nanofluid exhibited a concentration about 5% lower than the nanofluid. As *Ls* increased it suppressed mass diffusion by opposing or balancing diffusive transport, resulting in a slower increase in concentration.

- Effect of *k* and *We* on skin friction

Figure 6 shows the relationship between skin friction and *k* for *We*. A positive correlation indicated that skin friction increased with *k* for all *We*. Higher *We* values led to higher skin friction. It suggests that inertial forces dominate over surface tension at larger *We*. The hybrid nanofluid exhibited around 20% more skin friction than the nanofluid at *k* =0.4 for *We* = 5, and the absolute value of the skin friction coefficient rose linearly with the permeability parameter. At higher *We*, elastic forces dominated, further increasing skin friction. The separation between curves with *We* indicated its strong impact on fluid dynamics and stability.

- Effect of *k* and *Pr* on Nusselt number

Figure 7 presents the relationship between *Nu* and *k* for different *Pr*, in which *Nu* increased linearly with *k* for all *Pr* values, showing a direct relationship. Higher *Pr* values resulted in higher *Nu* values. Furthermore, the thermal diffusivity decreased relative to the momentum diffusivity as *Pr* increased. The hybrid nanofluid had a 15% higher heat transfer rate than the nanofluid at *k* = 0.3 for *Pr* = 8, and the *Nu* rose with increasing permeability parameter. Higher *Pr* values indicated a reduced thermal diffusivity relative to momentum diffusivity, enhancing heat transfer. The growing separation between curves with *Pr* reflects its more substantial influence on heat transfer.

- Effect of *k* and *Sc* on Sherwood numeral

The value of the *Sh* increased with *k* across all *Sc*, showing a positive correlation (Figure 8). As *Sc* increased from 1.0 to 1.5 at *k* = 0.3, the value of *Sh* increased by almost 30%. Increasing the *k* values enhanced convective mass transfer, further increasing *Sh* values. Higher *Sc* values indicated lower mass diffusivity, strengthening concentration gradients, and further boosting *Sh*. The analysis of various parameters contributes to the advancement of the biomedical industry, potentially enabling drug delivery to targeted sites using a base fluid.

6. Validation of the numerical and graphical results

To establish the accuracy and reliability of the present numerical procedure, a validation study was performed

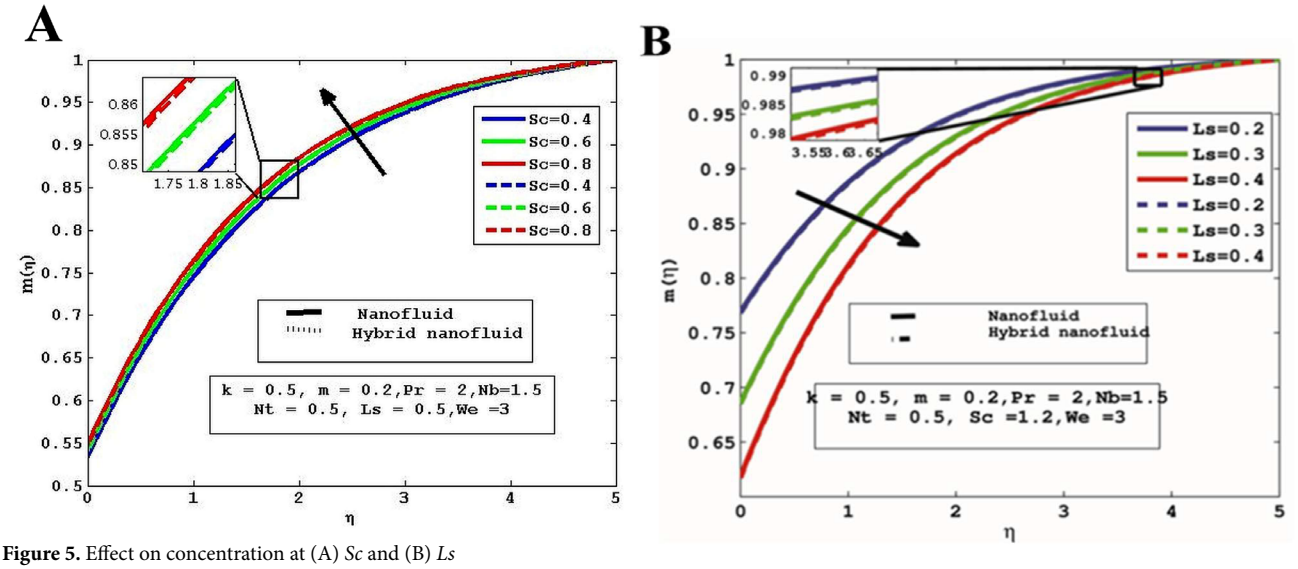


Figure 5. Effect on concentration at (A) *Sc* and (B) *Ls*

Abbreviations: *k*: curvature parameter; *Ls*: Homogeneous–heterogeneous reactions limiting factor; N_b: Brownian motion limiting factor; N_t: Thermophoresis limiting factor; *Pr*: Prandtl number; *Sc*: Schmidt number; *We*: Weissenberg number.

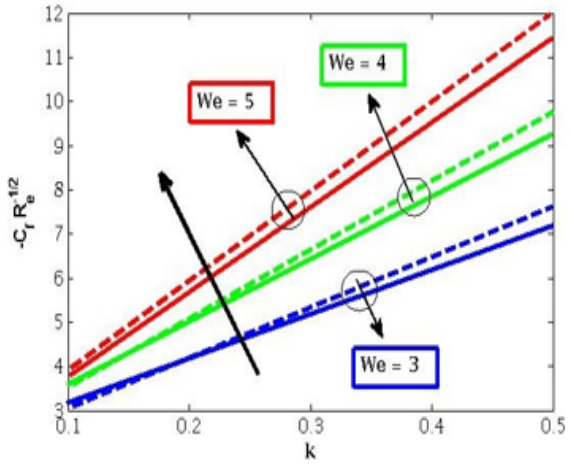


Figure 6. Effect of curvature parameter (k) on skin friction for various values of Weissenberg number (We)

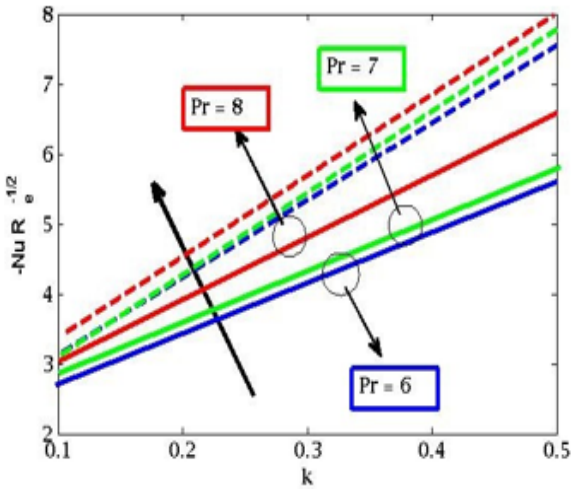


Figure 7. Effect of curvature parameter (k) and Prandtl number (Pr) on Nusselt numeral

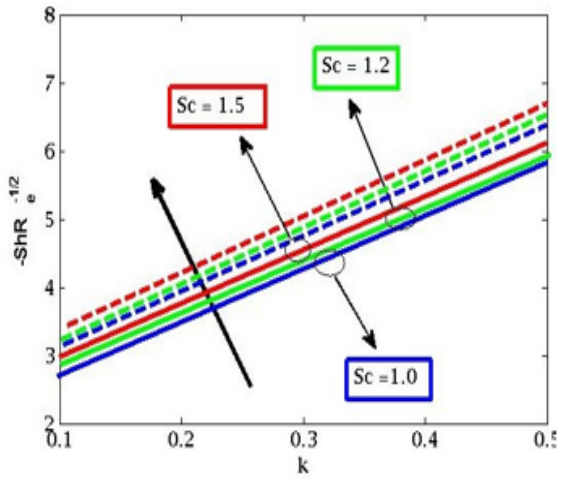


Figure 8. Effect of curvature parameter (k) and Schmidt number (Sc) on Sherwood numeral

by reducing the present mathematical model to an appropriate limiting case. The governing parameters associated with additional physical effects were set to zero or to their corresponding limiting values so that the resulting problem could be compared to previously published results. The present numerical results were then compared to the available literature values for the relevant engineering quantity. The comparison demonstrated close agreement between the present results and the published data, thereby confirming the accuracy of the MATLAB bvp5c implementation and the reliability of the numerical solutions obtained in the present investigation.

A comparative analysis was conducted against a previous study by Khan *et al.*,[17] which focused on homogeneous–heterogeneous reactions under different physical parameters, including velocity, temperature, concentration, local skin friction coefficient, and local *Nu*. In addition to another study by Benaissa *et al.*,[26] we focused on the application of each graphical application that contributed to wellness in the pharmaceutical and biomedical industry for different types of nanoparticles (Y_2O_3, ZrO_2).

7. Conclusion

In this study, the nonlinear convective flow of a Carreau hybrid nanofluid over an expanding exponential cylinder was numerically investigated, accounting for homogeneous–heterogeneous reactions, thermal radiation, and viscous dissipation. Similarity transformations were employed to reduce the governing equations to a system of nonlinear ordinary differential equations, which were solved using the MATLAB bvp5c solver. The results show that the governing physical parameters significantly influence the velocity, temperature, and concentration distributions. The inclusion of Y_2O_3–ZrO_2 Hybrid nanoparticles enhanced the heat-transfer characteristics, while viscous dissipation and thermal effects modified the temperature field. The homogeneous–heterogeneous reaction parameters substantially influenced the concentration distribution and mass-transfer behavior. The present findings provide useful theoretical insights into coupled heat and mass transport in Carreau hybrid nanofluids over expanding surfaces. Future investigations may consider experimental validation, transient and three-dimensional flow configurations, different nanoparticle morphologies, and more realistic physiological conditions to explore the potential biomedical relevance of the proposed model.

Acknowledgments

The authors sincerely acknowledge the support and facilities provided by their respective institutions, which enabled the successful completion of this research.

Funding

None.

Conflict of interest

The authors declare that they have no known competing financial interests or personal relationships that could have appeared to influence the work reported in this paper.

Author contributions

Conceptualization: Karthik Velusamy, Asaigeethan Palanisamy
Investigation: Shageen Fathima Shahul
Methodology: Karthik Velusamy
Formal analysis: Karthik Velusamy, Shageen Fathima Shahul
Writing – original draft: Karthik Velusamy
Writing – review & editing: Asaigeethan Palanisamy, Priya Arunkumar

Availability of data

Data are not openly available: Data are available upon reasonable request from the corresponding author.

References

1. Srinivasa Babu KS, Parandhama A, Bhuvana Vijaya R. Nonlinear MHD convective flow of Carreau nanofluid over an exponentially stretching surface with activation energy and viscous dissipation. *Nature*. 2021;3(3).

   doi: 10.1007/s42452-021-04339-4

2. Sarkar J, Ghosh P, Adil A. A review on hybrid nanofluids: Recent research, development and applications. *Renew Sustain Energy Rev.* 2015;43:164-177.

   doi: 10.1016/j.rser.2014.11.023

3. Suresh S, Venkitaraj KP, Selvakumar P, Chandrasekar M. Effect of Al_2O_3-Cu/water hybrid nanofluid in heat transfer. *Exp Therm Fluid Sci.* 2012;38:54-60.

   doi: 10.1016/j.expthermflusci.2011.11.007

4. Sidik NAC, Jamil MM, Japar WMAA, Adamu IM. A review on preparation methods, stability and applications of hybrid nanofluids. *Renew Sustain Energy Rev.* 2017;80:1112-1122.

   doi: 10.1016/j.rser.2017.05.221

5. Madhesh D, Kalaiselvam S. Experimental analysis of hybrid nanofluid as a coolant. *Procedia Eng.* 2014;97:1667-1675.

   doi: 10.1016/j.proeng.2014.12.317

6. Waqas M, Khan MI, Hayat T, Alsaedi A. Numerical simulation for magneto Carreau nanofluid model with

thermal radiation: A revised model. *Comput Methods Appl Mech Eng.* 2017;324:640-653.

doi: 10.1016/j.cma.2017.06.012

7. Eid MR, Mahny KL, Muhammad T, Sheikholeslami M. Numerical treatment for Carreau nanofluid flow over a porous nonlinear stretching surface. *Results Phys.* 2018;8:1185-1193.

doi: 10.1016/j.rinp.2018.01.070

8. Khan MI, Kumar A, Hayat T, Waqas M, Singh R. Entropy generation in flow of Carreau nanofluid. *J Mol Liq.* 2019;278:677-687.

doi: 10.1016/j.molliq.2018.12.109

9. Sardar H, Ahmad L, Khan M, Alshomrani AS. Investigation of mixed convection flow of Carreau nanofluid over a wedge in the presence of Soret and Dufour effects. *Int J Heat Mass Transfer.* 2019;137:809-822.

doi: 10.1016/j.ijheatmasstransfer.2019.03.132

10. Sulochana C, Ashwinkumar GP, Sandeep N. Transpiration effect on stagnation-point flow of a Carreau nanofluid in the presence of thermophoresis and Brownian motion. *Alexandria Eng J.* 2016;55(2):1151-1157.

doi: 10.1016/j.aej.2016.03.031

11. Khan SU, Shehzad SA. Electrical MHD Carreau nanofluid over porous oscillatory stretching surface with variable thermal conductivity: Applications of thermal extrusion system. *Phys A: Stat Mech Appl.* 2020;550:124132.

doi: 10.1016/j.physa.2020.124132

12. Alrehili M. Improvement for engineering applications through a dissipative Carreau nanofluid fluid flow due to a nonlinearly stretching sheet with thermal radiation. *Case Stud Therm Eng.* 2023;42:102768.

doi: 10.1016/j.csite.2023.102768

13. Shahid A, Bhatti MM, Ellahi R, Mekheimer KhS. Numerical experiment to examine activation energy and bi-convection Carreau nanofluid flow on an upper paraboloid porous surface: Application in solar energy. *Sustain Energy Technol Assess.* 2022;52:102029.

doi: 10.1016/j.seta.2022.102029

14. Irfan M, Rafiq K, Khan WA. Numerical analysis of unsteady Carreau nanofluid flow with variable conductivity. *Appl Nanosci.* 2020;10(8):3075-3084.

doi: 10.1007/s13204-020-01331-z

15. Ibrahim MG. Adaptive simulations to pressure distribution for creeping motion of Carreau nanofluid with variable fluid density effects: Physiological applications. *Therm Sci Eng Prog.* 2022;32:101337.

doi: 10.1016/j.tsep.2022.101337

16. Gireesha BJ, Kumar PBS, Mahanthesh B, Shehzad SA, Rauf A. Nonlinear 3D flow of Casson-Carreau fluids with homogeneous-heterogeneous reactions: A comparative study. *Results Phys.* 2017;7:2762-2770.

doi: 10.1016/j.rinp.2017.07.060

17. Khan I, Ullah S, Malik MY, Hussain A. Numerical analysis of MHD Carreau fluid flow over a stretching cylinder with homogeneous-heterogeneous reactions. *Results Phys.* 2018;9:1141-1147.

doi: 10.1016/j.rinp.2018.04.022

18. Ashraf BM, Haq SU. The convective flow of Carreau fluid over a curved stretching surface with homogeneous-heterogeneous reactions and viscous dissipation. *Waves Random Complex Media.* 2022;35(1):1483-1497.

doi: 10.1080/17455030.2022.2032867

19. Bibi A, Xu H. Peristaltic channel flow and heat transfer of Carreau magneto hybrid nanofluid in the presence of homogeneous/heterogeneous reactions. *Sci Rep.* 2020;10(1):11499.

doi: 10.1038/s41598-020-68409-0

20. Khan M, Ejaz S, Sardar H. Homogeneous-heterogeneous reactions in Carreau fluid flow with heat generation/absorption: Multiple solution. *J Braz Soc Mech Sci Eng.* 2019;41(11):490.

doi: 10.1007/s40430-019-1958-6

21. Hussain SM, Goud BS, Madheshwaran P, *et al*. Effectiveness of nonuniform heat generation (sink) and thermal characterization of a Carreau fluid flowing across a nonlinear elongating cylinder: A numerical study. *ACS Omega.* 2022;7(29):25309-25320.

doi: 10.1021/acsomega.2c02207

22. Azam M, Khan M, Alshomrani AS. Unsteady radiative stagnation point flow of MHD Carreau nanofluid over expanding/contracting cylinder. *Int J Mech Sci.* 2017;130:64-73.

doi: 10.1016/j.ijmecsci.2017.06.010

23. Siddiqa S, Molla M, Naqvi S. Carreau ferrofluid flow with inclined magnetic field in an enclosure having heated cylinder. *Phys Scr.* 2021;96(10):105007.

doi: 10.1088/1402-4896/ac0fd3

24. Lim YJ, Shafie S, Ullah I, Jamshed W, Eid MR, El Din SM. Effectiveness of non-uniform heat generation (sinking) and thermal characterization of Carreau fluid flowing across nonlinear elongating cylinder: Convergence analysis aspect. *J Appl Math Mech.* 2022.

doi: 10.1002/zamm.202200049

25. Rashad A, Nafe MA, Eisa D. 2D radiative Casson-Carreau hybrid nanofluid flow through a circular cylinder in a Darcy-Forchheimer porous medium. *New Valley Univ J*

Basic Appl Sci. 2023;1(1)1-19.

doi: 10.21608/nujbas.2023.218751.1012

26. Benaissa M, Ullah Z, Merga FE, *et al*. Variable density and chemical reaction effects on heat and mass transfer of magnetic second-grade nanofluid flow under slip conditions. *Discover Nano.* 2026;21:292.

doi: 10.1186/s11671-026-04746-9

27. Salih AAM, Ullah Z, Alamirew WD, *et al*. AI-driven oscillatory heat transfer efficiency in $MnZnFe_2O_4$-water nanofluid flow over solar collector plate with radiative source and exothermic reaction effects. *Discover Nano.* 2026;21:291.

doi: 10.1186/s11671-026-04758-5

28. Khedher NB, Ullah Z, Alamirew WD, et al. Graphene oxide nanoparticles oscillation in drilling fluid for heat transfer with entropy generation over radiative cylinder in fluctuating and laminar regimes. *Discover Nano.* 2026;21:165.

doi: 10.1186/s11671-026-04574-x

29. Ullah Z, Alam MM, Safdar F, Alosaimi M, Merga FE. Soret/Dufour, variable density, and viscous dissipation effects on heat and mass transfer of Oldroyd-B fluid flow over polymer sheet with convective heat flux. *AIP Adv.* 2025;15(5):055203.

doi: 10.1063/5.0257601

30. Krishnakanth D, Lakshminarayana P. Influence of thermal diffusion and molecular motion on heat transfer and fluid flow of Carreau ternary hybrid nanofluid. *Mod Phys Lett B.* 2026;40(7):2650028.

doi: 10.1142/S0217984926500284

31. Alarabi TH, Rashad AM, Mahdy A. Homogeneous-heterogeneous chemical reactions of radiation hybrid nanofluid flow on a cylinder with Joule heating: Nanoparticles shape impact. *Coatings.* 2021;11(12):1490.

doi: 10.3390/coatings11121490

32. Adeyemo AS, Sibanda P, Goqo SP. Analysis of heat and mass transfer of a nonlinear convective heat generating fluid flow in a porous medium with variable viscosity. *Sci Afr.* 2024;24:e02140.

doi: 10.1016/j.sciaf.2024.e02140

33. Ganji DD, Mahboobtosi M, Chari FN. Investigation of time-dependent magnetohydrodynamic flow and heat transfer of compressed penta-hybrid nanofluids: Biomedical applications. *J Radiat Res Appl Sci.* 2025;18(4):101915.

doi: 10.1016/j.jrras.2025.101915

34. Jamshed W, Nisar KS, Ibrahim RW, Mukhtar T, Vijayakumar V, Ahmad F. Computational framework of Cattaneo-Christov heat flux effects on engine oil-based Williamson hybrid nanofluids: A thermal case study. *Case Stud Therm Eng.* 2021;26:101179.

doi: 10.1016/j.csite.2021.101179

35. Turgut T, Tavman IH, Tavman S. Measurement of thermal conductivity of edible oils using transient hot wire method. *Int J Food Prop.* 2009;12(4):741-747.

doi: 10.1080/10942910802023242